RESEARCH ARTICLE | APRIL 24 2023

Pulsed laser ablation production of Ni/NiO nano electrocatalysts for oxygen evolution reaction

Iacono et al.

Valentina Iacono; Mario Scuderi; Maria Laura Amoruso; ... et. al

APL Energy 1, 016104 (2023)
https://doi.org/10.1063/5.0144600

Pulsed laser ablation production of Ni/NiO nano electrocatalysts for oxygen evolution reaction

Cite as: APL Energy 1, 016104 (2023); doi: 10.1063/5.0144600
Submitted: 31 January 2023 • Accepted: 30 March 2023 •
Published Online: 24 April 2023

Valentina Iacono[1,2] Mario Scuderi,[3] Maria Laura Amoruso,[3] Antonino Gulino[4,5] Francesco Ruffino[1,2,4] and Salvo Mirabella[1,2,a)]

AFFILIATIONS

[1] Dipartimento di Fisica e Astronomia "Ettore Majorana," Università di Catania, via S. Sofia 64, 95123 Catania, Italy
[2] CNR-IMM, Catania Università, via S. Sofia 64, 95123 Catania, Italy
[3] CNR-IMM, VIII strada 5, 95121 Catania, Italy
[4] Research Unit of the University of Catania, National Interuniversity Consortium of Materials Science and Technology (INSTM-UdR of Catania), Viale Andrea Doria 8 and Via S. Sofia 64, 95125 Catania, Italy
[5] Department of Chemical Sciences, University of Catania, Viale Andrea Doria 6, 95123 Catania, Italy

[a)] **Author to whom correspondence should be addressed:** salvo.mirabella@dfa.unict.it

ABSTRACT

Efficient and sustainable materials are requested to overcome the actual major issues related to green energy production. Ni/NiO nanoparticles (NPs, 2–4 nm in size) produced by Pulsed Laser Ablation in Liquid (PLAL) are reported as highly efficient and stable electrocatalysts for oxygen evolution reaction (OER) in water splitting applications. Ni/NiO NPs dispersions are obtained by ablating a Ni target immersed in deionized water with an Nd:YAG nanosecond pulsed laser. NPs size and density were driven by laser energy fluence (ranging from 8 to 10 J cm^{-2}) and shown to have an impact on OER performance. Ni/NiO NPs were characterized by scanning and transmission electron microscopy, x-ray diffraction, photoemission spectroscopy, and Rutherford back-scattering spectrometry. By drop-casting onto graphene paper, anode electrodes were fabricated for electrochemical water splitting in alkaline electrolytes. The extrinsic and intrinsic catalytic performances for OER have been quantified, achieving an overpotential of 308 mV (at a current density of 10 mA cm^{-2}) and unprecedented mass activity of more than 16 A mg^{-1}, using NPs synthesized with the highest and lowest laser energy fluence, respectively. The impact of NPs' size and density on OER performances has been clarified, opening the way for PLAL synthesis as a promising technique for highly efficient nano-electrocatalysts production.

I. INTRODUCTION

Over two centuries, the utilization of conventional fossil fuels has led to unsustainable oil use and significant pollution. Hence, the majority of countries are eager to develop an alternative supply of renewable energy.[1] Hydrogen has many favorable attributes, including an overall storage capacity, efficiency, renewability, cleanliness, massive distribution, high conversion, zero emissions, sources, versatility, and quick recovery, making it an excellent choice as an energy supply for heat and power, among many others.[2] From an electrochemical standpoint, hydrogen is unique in its ability to be cleanly and efficiently converted between chemical bonds and electrical energy, particularly at low temperatures. This conversion occurs in fuel cells as well as in water electrolyzers (water and electrical potential yields H_2 and O_2) through hydrogen and oxygen evolution reactions.[3] Among these two reactions, the oxygen evolution reaction (OER) typically requires critical materials and a large overpotential, limiting the efficiency of the overall water splitting.[4] Numerous efforts are being devoted to the design and synthesis of anodic materials that could substitute the best performing, but high cost, catalytic materials IrO_2 and RuO_2. Electrocatalysts with the first-row 3d transition metals (Ni, Fe, and Co) and their oxides/hydroxides have been recently investigated.[5–8] Competitive results have been obtained in terms of overpotential achieved at

a current density of 10 mA cm^{-2}. Unfortunately, these results are often achieved using high loadings of catalysts or increasing the electrode surface area, which allows to overcome the limited intrinsic catalytic activity of the electrocatalysts.[9]

Wide scientific attention has been devoted to lowering the overpotential needed for OER. However, the main goal is to get promising OER performance not only in terms of overpotential, but also in terms of intrinsic activity, using the lowest amount of catalyst possible. Thus, high mass activity (the ratio of current density to the catalyst loading mass) and low overpotential are both highly desirable. In this scenario, nanostructures can play a major role by improving the intrinsic utilization of the surface where catalysis occurs.

Beyond the electrode fabrication, the synthesis route of the nano-electrocatalyst should be considered. Typically, electrocatalyst fabrication needs laborious chemical methods with considerable by-products and waste.[10] Other synthesis techniques able to allow sustainable production of well-performing and stable electrocatalysts should be developed. Pulsed Laser Ablation in Liquid (PLAL) is a physical technique recently employed for solvent-free nanostructures (NSs) production.[11–14] This technique allows the preparation of metal oxides-based nanoparticles (NPs) by ablating a metallic target in an oxygen-rich liquid environment (i.e., deionized water). PLAL is a versatile technique that enables variation in the size and composition of the NPs produced by changing the synthesis parameters, such as the laser energy fluence and the liquid environment. Also, PLAL is considered an economically viable route for the fast and simple synthesis of NPs.[10] Recently, few works about nickel-based nano-electrocatalysts for water splitting obtained using PLAL have been reported.[15–18] Among these materials, nickel oxy-/hydroxide has been reported as a good electrocatalyst for OER in alkaline electrolytes. Nevertheless, the ablation is usually assisted with electrophoretic deposition, and a discussion about the effect of laser synthesis parameters on the intrinsic performance of the electrocatalysts is missing. Moreover, the inclusion of Fe has significantly increased the OER performance down shifting the overpotential.[19,20]

Here, we present the OER optimized performance of Ni/NiO NPs synthesized through pulsed laser ablation of a nickel target in deionized water. The effect of laser energy fluence on the morphological and structural properties of the NPs has been investigated. Moreover, a detailed study on the composition of the NPs has revealed a core–shell structure Ni/NiO and the presence of an external shell made of $NiOOH/Ni(OH)_2$. The overpotential and mass activity in OER electrochemical tests in alkaline electrolytes have been carefully quantified. The outcome of the electrochemical characterization highlights, at a current density of 10 mA cm^{-2}, an unprecedented mass activity ~16 A mg^{-1}, and overpotential of 308 mV vs reversible hydrogen electrode (RHE) using ~1 μg of Ni/NiO NPs obtained by PLAL.

II. EXPERIMENTAL SECTION

A. Synthesis of the Ni/NiO NPs

Ni/NiO nanoparticles (NPs) have been produced by PLAL. A pulsed (10 ns) Nd: YAG laser (Quanta-ray PRO-Series pulsed Nd: YAG laser), operating at a wavelength of 1064 nm, power 5 W, frequency 10 Hz, was used to ablate a nickel target (diameter 25 mm, thickness 0.1 mm, purity 99.99%) in de-ionized water (resistivity 18 MΩ cm). The high-power laser beam was focused through a convex lens (focal length 10 cm) on the nickel target placed at the bottom of a Teflon® cylindrical vessel (2.5 cm in diameter), filled with 8 ml of de-ionized water (Fig. 1). To vary the laser energy fluence onto the target, the focusing lens has been put at three distances (h = 8, 9, 10 cm) from the target.

The so-produced Ni/NiO dispersions were named with the value of h (e.g., PLAL-h8 refers to NPs produced with h = 8 cm). After 5 min of ablation, the produced Ni/NiO dispersion became gray colored, suggesting that a meaningful quantity of material was ablated. We weighted the Ni target before and after each ablation to extract the amount of ablated Ni. For this measurement, a microanalytical balance (Sartorius M5) with a sensitivity of 100 μg was used. The obtained solutions were stored at 4 °C.

B. Ni/NiO NPs characterization

The surface morphology of NPs and of the laser spot area on the Ni target were analyzed by using a Scanning Electron Microscopy (SEM) (Gemini field emission SEM Carl Zeiss SUPRA 25, FEG-SEM, Carl Zeiss Microscopy GmbH, Jena, Germany) combined with energy dispersive x-ray spectroscopy (EDX). EDX measurement was performed onto the electrode realized by the NPs dispersion dropped onto the silicon substrate in order to check any possible contamination (Fig. S3). Morphological characterization was done using a Transmission Electron Microscope (TEM) (2010F by JEOL, Akishima, Tokyo) operated in scanning TEM (STEM) mode at a primary beam energy of 200 keV. The NPs were prepared for TEM observation by drop casting the solution containing the NPs onto a Lacey carbon TEM grid. The micrographs were acquired using a high-angle annular dark-field (HAADF) detector, which provides bulk thickness contrast on the images (Z-contrast) for the STEM images. STEM images were analyzed by using DigitalMicrograph® software. The nanostructures' crystalline structure was investigated by X-Ray Diffraction (XRD) analysis, in grazing incidence mode (θ_{inc} = 0.2°) using a Smartlab Rigaku diffractometer, equipped with a rotating anode of CuK_α radiation (λ = 1.541 84 Å) operating at 45 kV and 200 mA. For this analysis, the Ni/NiO colloidal solution was drop-cast onto a Corning glass substrate and dried in ambient conditions. From XRD analysis, using the Reference Intensity Ratio (RIR) method, the weight ratio (%) of Ni and NiO was derived as described in the supplementary material. This was considered in estimating the catalyst loading starting from the Ni dose derived through Rutherford Backscattering Spectrometry (RBS) measurements. The surface composition of NPs was studied by performing x-ray photoelectron spectroscopy (XPS), at a 45° take-off angle relative to the surface sample holder, with a PHI 5000 Versa Probe II system (ULVAC-PHI, Inc., base pressure of the main chamber 1×10^{-8} Pa). Samples were excited with the monochromatized Al Kα x-ray radiation using a pass energy of 5.85 eV. The instrumental energy resolution was ≤0.5 eV. The XPS peak intensities were obtained after Shirley background removal.[21] Spectra calibration was achieved by fixing the graphene C 1s main peak at 284.6 eV. The catalyst loading mass was evaluated by performing Rutherford backscattering spectrometry (RBS, 2.0 MeV He^+ beam at normal incidence) with a 165° backscattering angle by using a 3.5 MV HVEE

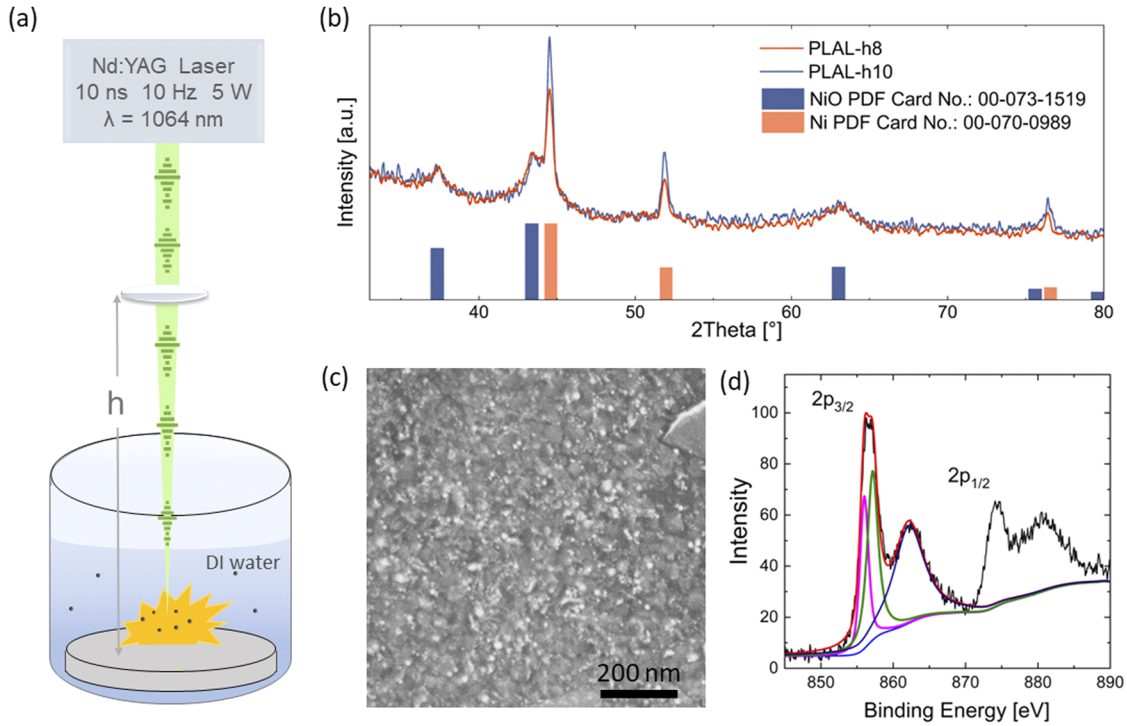

FIG. 1. (a) Schematic of PLAL apparatus. The Ni target immersed in DI water is ablated with the Nd:YAG nanosecond pulsed laser at different fluences obtained changing the distance (h = 8, 9, or 10 cm) between the focusing lens and the Ni target. (b) XRD pattern for the PLAL-h8 and PLAL-h10 samples presenting metallic Ni and NiO diffraction peaks. (c) SEM image of NiO-based NPs PLAL-h10 sample. (d) XPS Al-Kα excited XPS of PLAL-h10/GP sample in the Ni 2p binding energy region. The two peaks at 856.6 and 874.4 are consistent with the Ni $2p_{3/2,1/2}$ spin orbit components, and the two peaks at 862.1 and 880.8 are the related satellites.

Singletron accelerator system (High Voltage Engineering Europa, The Netherlands). RBS spectra were analyzed by using XRump software.[22]

C. Electrochemical analysis

Graphene paper (GP) (1 × 1.5 cm^2, 240 μm thick, Sigma-Aldrich, St. Louis, MO, USA) was rinsed with deionized water and dried in N_2 to clean its surface. To fabricate the electrodes, 60 μl of Ni/NiO dispersion has been drop cast onto the GP substrate. The electrodes were then dried on a hot plate at 80 °C for 1 h. Electrochemical analyses were performed using a Versastat-4 potentiostat in a three-electrode setup with a Pt wire as the cathode, a saturated calomel electrode (SCE) as the reference electrode, and the GP with the Ni/NiO NPs as the working electrode. All the measurements were performed at room temperature and atmospheric pressure, in a one-compartment electrochemical cell filled with 40 ml of aqueous 1M KOH (measured pH = 14) as the supporting electrolyte. Cyclic voltammetry (CV) curves were recorded at a scan rate of 10 mV s^{-1} in the potential range of 0–0.7 V vs SCE in order to stabilize the electrodes. The OER activities were investigated using linear sweep voltammetry (LSV) at a scan rate of 5 mV s^{-1} in the same potential windows of CVs. Electrochemical impedance spectroscopy (EIS) was performed with a superimposed 10 mV sinusoidal voltage in the frequency range of 10^4–10^{-1} Hz at a potential just after the onset potential (the minimum potential at which a reaction product is formed at an electrode). The extracted uncompensated resistance (R_u) was used to determine the iR drop.[23] For sample comparison, the value of the overpotential was taken at a current density of 10 mA cm^{-2}. Tafel plots were extrapolated from polarization curves by plotting the overpotential (η) as a function of the log of the current density. In order to evaluate the intrinsic catalytic activity, the Turnover Frequency (TOF) and the mass activity were evaluated. The TOF refers to the rate of production of oxygen molecules per active site and could be calculated as follows:

$$TOF = i/4nF \quad (s^{-1}), \tag{1}$$

where i is the measured current at a fixed overpotential, 4 are the electrons involved in the OER, F is the Faraday constant, and n is the number of moles of the active sites.[24] The number of moles of the active sites was derived from the electrocatalyst mass. The mass activity is defined as the ratio between the current density (10 mA cm^{-2}) and catalyst loading (mg) covering 1 cm^2 of the GP substrate. Chronopotentiometry (CP) analysis was carried out to study the stability of samples in an aqueous 1M KOH solution for 15 h at a constant current density of 10 mA cm^{-2}. For this long-term stability measurement, the CP was done using mercury/mercury oxide (Hg/HgO, saturated in 1M NaOH) as the reference electrode, to avoid the instability effect of the SCE.

III. RESULTS AND DISCUSSION

A. Synthesis and characterization of Ni/NiO NPs

Figure 1(a) shows the schematic of the PLAL process used for the synthesis of Ni/NiO NPs. The laser beam is focused by a lens onto a solid target in deionized water. The radiation absorbed by the target leads to the formation of an expanding plasma plume, which contains the ablated material and gives rise to a nanostructure dispersion.[12] In the schematic, the distance (h) between the lens and the target is varied. Figure S1 shows the circular laser spot obtained at h = 10 cm. The change in h leads the laser spot to change. For the three values of h, the measured area of laser spots is listed in Table I. The following equation reports how the fluence was evaluated:

$$F = \left(P / \dot{N}\right) / A \quad (\mathrm{J\ cm^{-2}}), \tag{2}$$

where F is the fluence, P is the mean output power of the laser measured with a power meter, $\dot{N}$ the number of pulses per second, and A the laser spot area.[12] By considering $\dot{N}$ = 10, and the mean output power 5 W, the fluence for each lens configuration was estimated.

In order to look at the structural properties of the nanostructures obtained at different fluences, the x-ray diffraction analysis was performed. In Fig. 1(b), we report the XRD characterization of nanostructures for the lowest (PLAL-h8) and the highest (PLAL-h10) fluences. The PLAL-h9 is reported and discussed in the supplementary material (Fig. S2). Both the XRD patterns exhibit two peaks at 44.60° and 51.98°, corresponding, respectively, to metallic Ni (111) and Ni (200) cubic structure (PDF Card No.: 00-070-0989) and two peaks at 37.33 and 43.38, corresponding, respectively, to NiO (111) and NiO (200) cubic structure (PDF Card No.: 00-073-1519). For all the samples, the FWHM of Ni peaks is smaller than that of NiO, pointing out that crystalline nickel should be bigger in size than the oxide, NiO, phase. Moreover, the intensity of Ni peaks is higher for PLAL-h10 in comparison to PLAL-h8. This could be associated with a higher amount of Ni in the PLAL-h10 sample. From XRD analysis, using the RIR method, the weight ratio (%) of Ni and NiO was derived as described in the supplementary material. This was considered in estimating the catalyst loading starting from the Ni dose derived through RBS measurements.

In Fig. 1(c), an SEM plan view image of the PLAL-h10 sample is reported. The image shows the presence of nanoparticles, typically with diameters of some tens of nanometers, covering the surface of GP. Figure S1 reports, for comparison, the SEM images of the PLAL-h8 [Fig. S1(b)], PLAL-h9 [Fig. S1(c)], and PLAL-h10 [Fig. S1(d)] samples. What emerges is the difference in the amount of ablated material dropped on the substrate surface. Indeed, the ablated mass measured with the microbalance resulted in 0.50 mg (PLAL-h8), 0.69 mg (PLAL-h9), and 0.87 mg (PLAL-h10). As we expected, by decreasing the fluence, a lower amount of target material is ablated. This effect, reported in the literature, is correlated with the lower temperature in the cavitation bubble, which decreases the ablation rate and leads to lower productivity.[10,25]

TABLE I. PLAL synthesis details reporting the fluence associated with each sample preparation and the amount of target ablated.

Sample	Laser spot area (mm^2)	Fluence ($J\ cm^{-2}$)	Ablated Ni (mg)
PLAL-h8	2.712	8.6	0.50
PLAL-h9	2.588	9.5	0.69
PLAL-h10	2.535	10.0	0.87

The composition of the NPs was investigated using energy dispersive x-ray spectroscopy. In particular, the assessment of the absence of Fe (or other elements) contamination was focused. In the EDX spectrum, reported in Fig. S3(a), the x-ray peaks associated with the Ni and O are visible and could be associated with the nanoparticles while Si peaks refer to the substrate. The EDX confirmed that no Fe traces are present in our system.

In order to analyze the surface properties of the nanoparticles, which significantly affect the electrochemical measurement, XPS measurement was performed. The Ni 2p peak shapes resulting from multiplet splitting, shake-up, and plasmon loss structures make challenging the XPS analysis of mixed metal, metal oxide, and hydroxide systems.[26] Figure 1(d) shows the high-resolution of the PLAL-h10 sample in the Ni 2p binding energy (B.E.) region. The Ni $2p_{3/2}$ spectrum was first deconvoluted with the superposition of three components at 855.9, 857.1, and 862.1 eV. According to the very recent related reports, the first component accounts for $Ni(OH)_2$ (39%), the second component is consistent with the presence of NiOOH (61%), and the third component is a satellite peak characteristic of Ni (II).[27] In Fig. S3(b), a deeper spectral fitting of the high-resolution Ni 2p B.E., which required seven Gaussian components, resulted in an agreement with the γ-NiOOH envelope.[28]

Thus, XPS revealed that the surface of the PLAL-NPs is composed of a mixture of the two oxides, mostly of Ni^{3+}. Unlike XRD, XPS sample depth is of few nanometers. The two techniques are complementary. XRD showed that the bulk of the NPs are made of Ni and NiO and XPS revealed that their surface has an oxy-/hydroxide shell. The hydroxide shell could be due to the liquid media in which the obtained NPs' dispersion is synthetized.[25]

TEM analysis gave us information on the structure of the nanoparticles and let us extract the particle-size distribution (PSD). Figures 2(a) and 2(b) show the STEM Z-contrast images of PLAL-h8 and PLAL-h10 samples. Mostly, the nanoparticles (circled with white gray dashed lines) show a core–shell structure. According to XRD, the Ni core is mainly bigger in the PLAL-h10 sample. The thickness of the oxide shell extracted from the bigger NPs is ~3.5 nm. Looking at other works reporting the PLAL synthesis of NPs ablating a Ni target in water, the core–shell structures are typically obtained for those NPs having a diameter higher than 8 nm.[29,30] Thus, according to XRD and XPS analyses, we can suppose NPs as schematized in Fig. 2(c): a Ni core is surrounded by a NiO shell, and a second shell is made up of a mixture of the two Ni oxy-/hydroxides species. Figure 2(d) reports the PSD measured over more than 450 nanoparticles. The PSD has been obtained considering a lognormal distribution.[29] Thus, the mode and the FWHM of the main peak of the distribution have been derived. The most representative size (MRS) is 2.4 nm for PLAL-h8 and 3.4 nm for PLAL-h10. The width of the PLAL-h10 distribution is larger than that of PLAL-h8. This higher spread in the distribution of NPs was also reported in a previous study of Lasemi *et al.*[31] studying the effect of laser fluence on Ni-based NPs size distribution. It was seen that increasing the fluence, the median size and the size distribution width increased

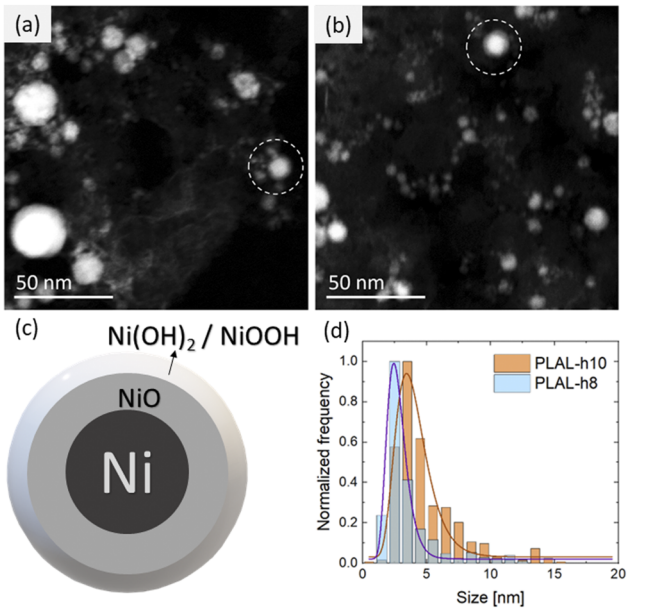

FIG. 2. (a) and (b) STEM Z-contrast images of PLAL-h8 and PLAL-h10 nanoparticles, respectively. Dashed circles evidence the core–shell structure of some nanoparticles. (c) NPs structure scheme: Ni core with a primary NiO shell and an oxide/hydroxide NiOOH/$Ni(OH)_2$ superficial shell. (d) PSD of PLAL-h8 and PLAL-h10 nanoparticles. The size value is reported in nm. The curves used for the analysis are lognormal.

too. At high fluence, larger NPs are formed because more energy is involved in the ablation, leading to enhanced aggregation and coalescence processes.[25]

B. Electrochemical measurements

To measure the performances of NiO-based NPs electrocatalysts toward the OER, we performed electrochemical measurements in alkaline media (aqueous 1M KOH, pH 14) according to the procedure shown in the Experimental section. First, stabilization through the CV technique was done.

In Fig. 3(a), we report the LSV. The potential values (vs RHE) are iR drop free. The iR was extrapolated from the Nyquist plot [Fig. S3(a)] acquired as described in the Experimental section. The Nyquist plots obtained were fitted with the equivalent circuit of Armstrong and Henderson represented as an inset in Fig. S3(a). The elements of the circuit model are explained in the supplementary material, and the fitting parameters obtained are reported in Table S1. The current density was evaluated considering that the immersed area of the electrode was 1 cm^2. The OER performance was also evaluated for the bare GP as it allows oxygen reactions. The LSV plot reveals that the GP loaded with the NPs starts the oxygen evolution reaction at well lower potential compared to the GP alone, evidencing the catalytic activity of our NPs. For the bare GP, the value of overpotential at 10 mA cm^{-2} of the substrate was 362 mV. The value of overpotential at 10 mA cm^{-2} obtained for the samples was: 308 mV (PLAL-h10), 309 mV (PLAL-h9), and 312 mV (PLAL-h8). The lowest value was reached by the PLAL-h10 sample.

The kinetics study was performed by evaluating the Tafel slope from the LSV measurements. In Fig. 3(b), the Tafel plot shows the slopes for the three samples, always in the 40–55 mV dec^{-1} range. A detailed study reported by Shinagawa suggests that a value of Tafel slope ~40 mV/dec indicates that the rate determining step in OER reaction is the adsorption of OH^- ions onto the electrocatalysts surface. All three samples show similar Tafel slopes that slowly increase at higher currents. As a matter of fact, at a higher current, the adsorption sites for the OH^- ions begin to be occupied leading to an increase in the Tafel slope value.[15,32]

As the overpotential is generally considered an extrinsic parameter for the OER process, we turned our attention to evaluating the intrinsic catalytic activity indicators for our electrocatalysts. The TOF and the mass activity evaluation are based on catalyst loading quantification.[9] In our case, the NPs mass is well lower than the typical analytical balance so an advanced methodology must be used. RBS analysis was employed to determine the catalyst mass exploiting the accuracy of this ion-beam based material science technique.[33] In Fig. 4(a), the inset shows a schematic of RBS measurement. E_0 is the energy of the incident He^+ ion beam, and E_1 is theenergy (measured by a Si detector at 15° off the normal incident beam direction)

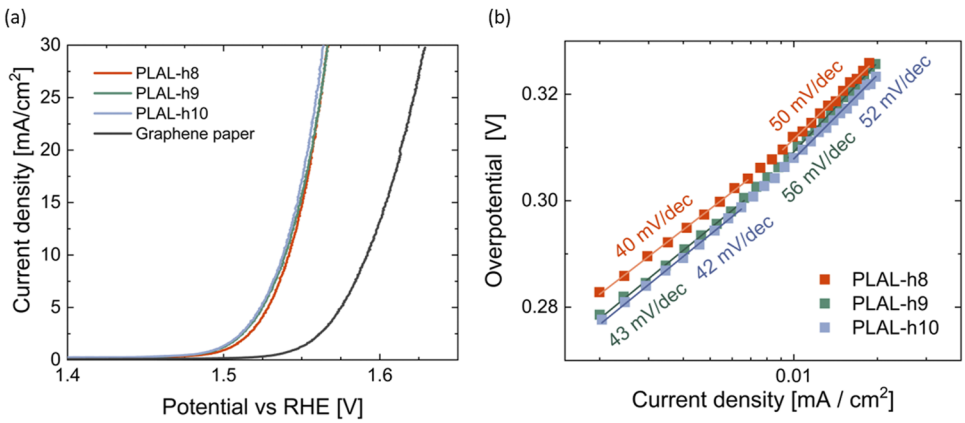

FIG. 3. (a) LSV curves of the three electrodes and the bare GP obtained in aqueous 1M KOH at a scan rate of 5 mV s^{-1} corrected with the iR drop. (b) Tafel plot obtained from the LSV measurements for the Ni/NiO NPs loaded on GP. For each electrode, with the same legend color, the Tafel slopes are reported.

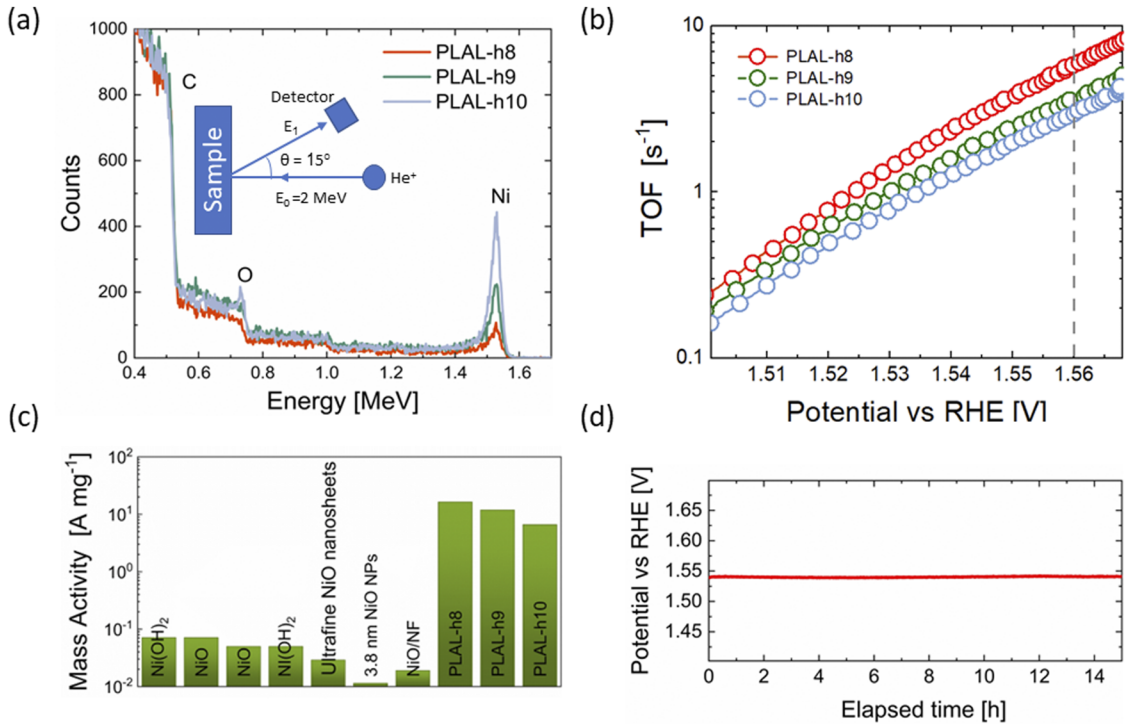

FIG. 4. (a) RBS spectra of the three NP-based electrodes. In the spectra, for each peak signal, the correspondent element is indicated. The drawing shows the technique setup. (b) TOF varies with the potential vs RHE. The dashed gray line is at η = 330 mV. (c) Comparison of mass activity values at 10 mA cm^{-2} for NiO-based electrocatalysts.[43–47] (d) Chronopotentiometry performed for the PLAL-h10 electrode for 15 h at 10 mA cm^{-2} current density.

of He^+ backscattered by each element on the surface. The spectra show the presence of Ni, O, and C element, with the signal starting at energy E_1 of 1.53, 0.73, and 0.51 MeV, respectively. The area below the Ni peak is related to the number of scattering centers (Ni atoms per cm^2). For the catalyst loading calculation, the Ni and NiO fraction was estimated with the RIR method from the XRD analysis (see the supplementary material). In Table II, we resume the weight ratio found for each NP's dispersion by the RIR method and the catalyst mass.

The PLAL-h10 electrode contains almost three times more catalyst mass compared to the PLAL-h8. This confirms the effect of laser fluence on the NP productivity: at higher laser fluence, the ablated mass by target increased by a factor of 1.7, but the NP amount increased by two times. Assuming that all the catalysts are electrochemically active, a TOF value has been estimated [Eq. (1)] for a range of potentials approximately to $\eta_{10\ \mathrm{mA\ cm^{-2}}}$. Figure 4(b) shows the three TOF curves in the range of 1.50–1.57 V vs RHE. The dashed gray line refers to an overpotential value of 330 mV. Increasing the potential, the TOF values increase too, as the current increases. PLAL-h8 electrode possesses higher values of TOF, imputable to better catalyst utilization. As shown in Table III, the value of the highest TOF is referred to the sample with the lowest mass loading. For our work, even though the PLAL-h10 electrode is loaded with more catalysts, not all the material provides electrochemically active sites for OER. The mass activity of each electrode was calculated at 10 mA cm^{-2}. Such a feature for the PLAL-h8 sample (more than 16 A mg^{-1}) is the largest among other Ni/NiO-based electrocatalysts. While PLAL-h10 electrode exposes more catalytic sites (allowing a reduced overpotential), it seems that not the whole loaded catalyst actively participates in the oxygen production, thus giving a reduced mass activity. These results suggest that despite the very low amount of loaded catalyst, the PLAL-based Ni/NiO NPs are highly electrochemically active, allowing them to reach 10 mA cm^{-2} at a very low overpotential for OER. Figure S4(b) shows TOF values for other NiO-based electrocatalysts.[36,41,42] Many works report this value at different overpotentials, such as 350 mV, and typically have values of 10^{-1}–10^{-2} s^{-1}. Our results show higher TOF at lower overpotential (330 mV vs RHE). Figure 4(c) shows the mass activity of some NiO-based electrocatalysts.[43–47] The OER activity is indeed

TABLE II. Structural and morphological parameters for each synthesis condition and catalyst loading for each electrode.

Sample	h (cm)	Fluence (J cm^{-2})	MRS (nm)	W_{Ni} (%)	W_{NiO} (%)	Catalyst loading (μg cm^{-2})
PLAL-h8	8	8.6	2.4	0.49	0.51	0.7
PLAL-h9	9	9.5	···	0.57	0.43	1.1
PLAL-h10	10	10	3.4	0.55	0.45	1.4

TABLE III. NiO-based electrocatalysts OER comparison in aqueous 1M KOH. Mass activity is reported at 10 mA cm^{-2}.

Sample	Catalyst loading ($\mu g/cm^2$)	Overpotential (mV)	Tafel slope (mV dec^{-1})	TOF (s^{-1})	Mass activity (A/mg)	Reference
NiO nanosheets	300	340	97	···	0.03	34
3-D-PC-G @NiO NS	300	320	52	···	0.03	35
NiO microflowers	500	314	47	0.01 @ 350 mV	0.02	36
Freeze-dried NiO	···	309	40	1.27 @ 270 mV	···	37
NiO NPs/rGO	···	369	48	0.2 @ 400 mV	···	38
Ni/NiO NPs	···	320	61	0.11 @ 350 mV	···	39
2h-Ni/NiO SPE	4.0	231	108	0.02 @ 350 mV	2.5	40
PLAL $Ni(OH)_2$ NPs	···	2017	73	···	···	17
PLAL-h8	0.7	312	40	6.0 @ 330 mV	16.4	This work
PLAL-h9	1.1	309	43	3.6 @ 330 mV	11.9	This work
PLAL-h10	1.4	308	42	3.0 @ 330 mV	6.6	This work

strictly dependent on the surface properties of the electrocatalysts. It has been reported that NiOOH is a highly efficient OER catalyst. The difference in OER activity between NiO and $Ni(OH)_2$/NiOOH-based catalysts has been widely discussed in the literature involving a discussion on surface energies and defect structures, which varies depending on the synthesis process actuated.[48,49] NiOOH has been found to have a layered double hydroxide structure, which due to large intersheet spacing could better the transfer of electrons and hydroxide groups between its structure.[50]

The stability of electrodes was tested with a chronopotentiometry analysis for 15 h at a constant current density of 10 mA cm^{-2}. The measurement result, shown in Fig. 4(d), indicates only an increase of the potential of 0.1% after 15 h of OER activity.

Even if our electrodes are loaded with few catalysts, this is sufficient in order to reach a competitive and stable OER performance with the literature.

Once the electrochemical test was done, we investigated possible composition changes in the nanostructures due to the OER reaction. We repeated the XPS measurement to a PLAL-h10 electrode after OER testing. As shown in Fig. S7, the Ni 2p binding energy region of the deconvoluted component at 854.7 eV is due to $Ni(OH)_2$ (51%) and that at 855.8 eV is due to the NiOOH species (49%).

Compared to the sample before the OER, the percentage of $Ni(OH)_2$ increased. The difference in the $Ni(OH)_2$/NiOOH ratio agrees with its use for oxygen evolution. This was generally observed in testing NiO-based electrocatalysts after OER activity in which the $Ni(OH)_2$ percentage increases.[18,51] XPS analysis was also performed after the electrolysis in order to check the possible Fe contamination. Figure S7 reports the XPS spectrum including the Fe region and confirms that no Fe is present after electrolysis. Thus, the performance obtained is due to only Ni/NiO NPs over the GP substrate.

IV. CONCLUSIONS

In conclusion, we showed how PLAL allows the synthesis of highly active and stable OER electrocatalysts based on Ni/NiO nanoparticles (2–4 nm in size) with an oxy-/hydroxide surface shell. By varying the laser energy fluence, different water-based NPs dispersions were obtained and used to produce water-splitting electrodes by drop casting onto graphene paper substrate. At a current density of 10 mA cm^{-2}, an overpotential of 308 mV for OER was achieved by using only 1–2 μg cm^{-2} of Ni/NiO catalyst obtained at the 10 J cm^{-2} laser fluence. Careful quantification of catalyst loading allowed us to measure an unprecedented mass activity higher than 16 A mg^{-1} for Ni/NiO catalyst synthesized at the lowest laser fluence value, for which smaller NP sizes are obtained. The high mass activity and the promising overpotential achieved by these electrocatalysts obtained by PLAL pave the way for sustainable synthesis of highly efficient OER catalysts needed for scaling-up in water-splitting application.

SUPPLEMENTARY MATERIAL

See the supplementary material for additional information described in this paper.

ACKNOWLEDGMENTS

This work was supported by the project "Programma di ricerca di ateneo UNICT 2020–22 linea 2" of the University of Catania, Italy. This work was partially funded by European Union (NextGeneration EU), through the MUR-PNRR project SAMOTHRACE (Grant No. ECS00000022). The authors thank the Bio-nanotech Research and Innovation Tower (BRIT) laboratory of the University of Catania (Grant No. PONa3_00136 financed by the MIUR) for the Smartlab diffractometer facility and Professor G. Malandrino (uniCT) for kind availability related to XRD measurements; Professor E. Bruno for her support in the synthesis method approach; and S. Tatì, C. Percolla, and G. Pantè (CNR-IMM, Catania University, Italy) for technical support.

AUTHOR DECLARATIONS

Conflict of Interest

The authors have no conflicts to disclose.

Author Contributions

Valentina Iacono: Data curation (equal); Formal analysis (equal); Investigation (equal); Methodology (equal); Writing – original draft (equal); Writing – review & editing (equal). **Mario Scuderi**: Data curation (equal); Formal analysis (equal); Investigation (equal); Methodology (equal); Writing – review & editing (equal). **Maria Laura Amoruso**: Formal analysis (equal); Methodology (equal); Writing – review & editing (equal). **Antonino Gulino**: Data curation (equal); Formal analysis (equal); Investigation (equal); Methodology (equal); Writing – original draft (equal); Writing – review & editing (equal). **Francesco Ruffino**: Conceptualization (equal); Data curation (equal); Formal analysis (equal); Funding acquisition (equal); Investigation (equal); Methodology (equal); Resources (equal); Supervision (equal); Writing – review & editing (equal). **Salvo Mirabella**: Conceptualization (equal); Funding acquisition (equal); Investigation (equal); Methodology (equal); Supervision (equal); Writing – review & editing (equal).

DATA AVAILABILITY

The data that support the findings of this study are available within the article and its supplementary material.

REFERENCES

[1] U. Y. Qazi, Energies **15**(13), 4741 (2022).
[2] R. Javaid, Catalysts **11**(7), 836 (2021).
[3] B. Pivovar, N. Rustagi, and S. Satyapal, Electrochem. Soc. Interface **27**, 47 (2018).
[4] A. Alobaid, C. Wang, and R. A. Adomaitis, J. Electrochem. Soc. **165**, J3395 (2018).
[5] G. Zhang, J. Zeng, J. Yin, C. Zuo, P. Wen, H. Chen, and Y. Qiu, Appl. Catal., B **286**, 119902 (2021).
[6] J. Qi, W. Zhang, and R. Cao, ChemCatChem **10**(6), 1206 (2018).
[7] F. Lyu, Q. Wang, S. M. Choi, and Y. Yin, Small **15**(1), 1804201 (2019).
[8] B. M. Hunter, H. B. Gray, and A. M. Müller, Chem. Rev. **116**, 14120 (2016).
[9] J. Kibsgaard and I. Chorkendorff, Nat. Energy **4**(6), 430 (2019).
[10] D. Zhang, B. Gökce, and S. Barcikowski, Chem. Rev. **117**(5), 3990 (2017).
[11] S. Barcikowski, V. Amendola, G. Marzun, C. Rehbock, S. Reichenberger, D. Zhang, and B. Gokce, *Handbook of Laser Synthesis & Processing of Colloids*, 2nd ed. (Duisburg-Essen Publications Online, 2019).
[12] M. Censabella, V. Torrisi, S. Boninelli, C. Bongiorno, M. G. Grimaldi, and F. Ruffino, Appl. Surf. Sci. **475**, 494 (2019).
[13] R. C. Forsythe, C. P. Cox, M. K. Wilsey, and A. M. Müller, Chem. Rev. **121**(13), 7568 (2021).
[14] V. Amendola, D. Amans, Y. Ishikawa, N. Koshizaki, S. Scirè, G. Compagnini, S. Reichenberger, and S. Barcikowski, Chem. - Eur. J. **26**(42), 9206 (2020).
[15] T. Begildayeva, D. Chinnadurai, S. J. Lee, Y. Yu, J. K. Song, and M. Y. Choi, J. Alloys Compd. **901**, 163446 (2022).
[16] A. V. Shabalina, V. A. Svetlichnyi, and S. A. Kulinich, Curr. Opin. Green Sustainable Chem. **33**, 100566 (2022).
[17] A. Shukla, S. C. Singh, C. S. Saraj, G. Verma, and C. Guo, Mater. Today Chem. **23**, 100691 (2022).
[18] C. S. Saraj, S. C. Singh, A. Shukla, W. Yu, M. U. Fayyaz, and C. Guo, ChemElectroChem **8**(1), 209 (2021).
[19] B. M. Hunter, J. D. Blakemore, M. Deimund, H. B. Gray, J. R. Winkler, and A. M. Müller, J. Am. Chem. Soc. **136**, 13118 (2014).
[20] B. M. Hunter, W. Hieringer, J. R. Winkler, H. B. Gray, and A. M. Müller, Energy Environ. Sci. **9**, 1734 (2016).
[21] D. A. Shirley, Phys. Rev. **5**, 4709 (1972).
[22] M. Thompson, https://www.genplot.com.
[23] S. Anantharaj, S. R. Ede, K. Karthick, S. Sam Sankar, K. Sangeetha, P. E. Karthik, and S. Kundu, Energy Environ. Sci. **11**(4), 744 (2018).
[24] S. Anantharaj, P. E. Karthik, and S. Noda, Angew. Chem., Int. Ed. **60**(43), 23051 (2021).
[25] N. Lasemi and G. Rupprechter, Catalysts **10**(12), 1453 (2020).
[26] M. C. Biesinger, B. P. Payne, L. W. M. Lau, A. Gerson, and R. S. C. Smart, Surf. Interface Anal. **41**(4), 324 (2009).
[27] D. Rathore, A. Banerjee, and S. Pande, ACS Appl. Nano Mater. **5**(2), 2664 (2022).
[28] A. P. Grosvenor, M. C. Biesinger, R. S. C. Smart, and N. S. McIntyre, Surf. Sci. **600**(9), 1771 (2006).
[29] H. J. Jung and M. Y. Choi, J. Phys. Chem. C **118**(26), 14647 (2014).
[30] R. Mahfouz, F. J. Cadete Santos Aires, A. Brenier, B. Jacquier, and J. C. Bertolini, Appl. Surf. Sci. **254**, 16, 5181 (2008).
[31] N. Lasemi, U. Pacher, C. Rentenberger, O. Bomatí-Miguel, and W. Kautek, ChemPhysChem **18**(9), 1118 (2017).
[32] T. Shinagawa, A. T. Garcia-Esparza, and K. Takanabe, Sci. Rep. **5**, 13801 (2015).
[33] P. Malinský, V. Hnatowicz, and A. Macková, Nucl. Instrum. Methods Phys. Res., Sect. B **371**, 101 (2016).
[34] J. Dandan, G. Hongyi, X. Liwen, C. Xiao, D. Wenjun, H. Xiubing, and W. Ge, Inorg. Chem. **58**(10), 6758 (2019).
[35] W. Yuan, C. Li, M. Zhao, J. Zhang, C. M. Li, and S. P. Jiang, Electrochim. Acta **342**, 136118 (2020).
[36] L. Bruno, M. Scuderi, F. Priolo, and S. Mirabella, Sustainable Energy Fuels **6**, 4498 (2022).
[37] Y. Shudo, M. Fukuda, Md. S. Islam, K. Kuroiwa, Y. Sekine, M. R. Karim, and S. Hayami, Nanoscale **13**(10), 5530 (2021).
[38] S. G. Jo, C.-S. Kim, S. J. Kim, and J. W. Lee, Nanomaterials **11**(12), 3379 (2021).
[39] F. E. Sarac Oztuna, T. Beyazay, and U. Unal, J. Phys. Chem. C **123**, 28131 (2019).
[40] S. N, J. P. Hughes, P. S. Adarakatti, M. C, S. J. Rowley-Neale, A. S, and C. E. Banks, RSC Adv. **11**, 14654–14664 (2021).
[41] V. D. Silva, T. A. Simões, J. P. F. Grilo, E. S. Medeiros, and D. A. Macedo, J. Mater. Sci. **55**, 6648 (2020).
[42] A. C. Pebley, E. Decolvenaere, T. M. Pollock, and M. J. Gordon, Nanoscale **9**, 15070 (2017).
[43] L.-A. Stern, L. Feng, F. Song, and X. Hu, Energy Environ. Sci. **8**(8), 2347 (2015).
[44] X.-Y. Yu, Y. Feng, B. Guan, X. W. Lou, and U. Paik, Energy Environ. Sci. **9**(4), 1246 (2016).
[45] Y. Zhao, X. Jia, G. Chen, L. Shang, G. I. N. Waterhouse, L.-Z. Wu, C.-H. Tung, D. O'Hare, and T. Zhang, J. Am. Chem. Soc. **138**(20), 6517 (2016).
[46] K. Fominykh, P. Chernev, I. Zaharieva, J. Sicklinger, G. Stefanic, M. Döblinger, A. Müller, A. Pokharel, S. Böcklein, C. Scheu, T. Bein, and D. Fattakhova-Rohlfing, ACS Nano **9**(5), 5180 (2015).
[47] Q. Zhang, C. Zhang, J. Liang, P. Yin, and Y. Tian, ACS Sustainable Chem. Eng. **5**(5), 3808 (2017).
[48] Y.-F. Li, J.-L. Li, and Z.-P. Liu, J. Phys. Chem. C **125**, 27033 (2021).
[49] Y. Chen, K. Rui, J. Zhu, S. X. Dou, and W. Sun, Chem. - Eur. J. **25**(3), 703 (2018).
[50] L.-A. Stern and X. Hu, Faraday Discuss. **176**, 363 (2014).
[51] M. Urso, G. Torrisi, S. Boninelli, C. Bongiorno, F. Priolo, and S. Mirabella, Sci. Rep. **9**, 7736 (2019).